redshift of $z = 0.6799 \pm 0.0001$. We also obtained spectra of two faint galaxies immediately to the southwest of component G (Fig. 2) using the Faint Object Camera and Spectrograph[26] of the Subaru telescope. The redshifts of these two faint galaxies are $z = 0.6751 \pm 0.0001$, strongly suggesting a cluster of galaxies at $z \approx 0.68$ centred on component G. Clusters are dominated by elliptical galaxies, which all have very similar spectral energy distributions.

Many of the faint galaxies in Fig. 2 ($\sim$40 galaxies around component G) have colours that are similar to that of component G. The colours are consistent with the expected colours of elliptical galaxies at $z \approx 0.68$ ($g - r \approx 1.8$ and $r - i \approx 1.1$). In addition, there is an X-ray source in this direction detected by the ROSAT All-Sky Survey[27] (0.236 counts per second in a 473-s exposure). The emission, however, comes most probably from the quasar, because the detected X-ray flux is too strong for typical clusters of galaxies at $z = 0.68$. Finally, we note two possible arclets (highly distorted images of background galaxies due to gravitational lensing) in Fig. 2 (marked as 'arc?') close to component D. If future observations confirm that the arclets are indeed lensed background galaxies, they will provide strong additional constraints on the total mass distribution of the lensing cluster.

The lensing interpretation is further supported by a theoretical model of SDSS J1004+4112. We fitted the positions of the four quasar components with a singular isothermal ellipsoid (SIE) plus external shear model using lens modelling software[28]. The best-fit model is illustrated in Fig. 3. The positions and relative brightnesses of all components agree well with the lens model predictions. The centre of the lensing mass is offset from the centre of component G by about 10 kpc at the cluster redshift, but the brightest galaxy of a cluster is not always found exactly at the centre of the potential well of that cluster.

The identical redshifts ($z = 1.734$) and the spectral energy distributions of the four lensed components, the existence of a lensing cluster of galaxies ($z = 0.68$), and the presence of possible arclets confirm the hypothesis that the quasar is lensed by this cluster. Furthermore, a theoretical lensing model involving the cluster and external shear simultaneously accounts for the observed geometry of the system and the relative brightness of the images. The present work represents the discovery of a long-predicted but previously undetected population of large-separation lensed quasars. □

Received 30 July; accepted 23 October 2003; doi:10.1038/nature02153.

1. Narayan, R. & White, S. D. M. Gravitational lensing in a cold dark matter universe. *Mon. Not. R. Astron. Soc.* **231,** 97–103 (1988).
2. Wambsganss, J., Cen, R., Ostriker, J. P. & Turner, E. L. Testing cosmogonic models with gravitational lensing. *Science* **268,** 274–276 (1995).
3. Keeton, C. R. & Madau, P. Lensing constraints on the cores of massive dark matter halos. *Astrophys. J.* **549,** L25–L28 (2001).
4. Wyithe, J. S. B., Turner, E. L. & Spergel, D. N. Gravitational lens statistics for generalized NFW profiles: Parameter degeneracy and implications for self-interacting cold dark matter. *Astrophys. J.* **555,** 504–523 (2001).
5. Takahashi, R. & Chiba, T. Gravitational lens statistics and the density profile of dark halos. *Astrophys. J.* **563,** 489–496 (2001).
6. Oguri, M. Constraints on the baryonic compression and implications for the fraction of dark halo lenses. *Astrophys. J.* **580,** 2–11 (2002).
7. Navarro, J. F., Frenk, C. S. & White, S. D. M. A universal density profile from hierarchical clustering. *Astrophys. J.* **490,** 493–508 (1997).
8. Maoz, D., Rix, H., Gal-Yam, A. & Gould, A. Survey for large-image separation lensed quasars. *Astrophys. J.* **486,** 75–84 (1997).
9. Ofek, E. O., Maoz, D., Prada, F., Kolatt, T. & Rix, H. A survey for large-separation lensed FIRST quasars. *Mon. Not. R. Astron. Soc.* **324,** 463–472 (2001).
10. Phillips, P. M. *et al.* The JVAS/CLASS search for 6-arcsec to 15-arcsec image separation lensing. *Mon. Not. R. Astron. Soc.* **328,** 1001–1015 (2001).
11. Zhdanov, V. I. & Surdej, J. Quasar pairs with arcminute angular separations. *Astron. Astrophys.* **372,** 1–7 (2001).
12. Kochanek, C. S. *et al.* CASTLES survey. ⟨http://cfa-www.harvard.edu/castles/⟩ (2003).
13. Walsh, D., Carswell, R. F. & Weymann, R. J. 0957+561 A, B — Twin quasistellar objects or gravitational lens? *Nature* **279,** 381–384 (1979).
14. Colley, W. N., Tyson, J. A. & Turner, E. L. Unlensing multiple arcs in 0024+1654: Reconstruction of the source image. *Astrophys. J.* **461,** L83–L86 (1996).
15. Turner, E. L., Ostriker, J. P. & Gott, J. R. III The statistics of gravitational lenses—the distributions of image angular separations and lens redshifts. *Astrophys. J.* **284,** 1–22 (1984).
16. York, D. G. *et al.* The Sloan Digital Sky Survey: Technical summary. *Astron. J.* **120,** 1579–1587 (2000).
17. Stoughton, C. *et al.* Sloan Digital Sky Survey: Early data release. *Astron. J.* **123,** 485–548 (2002).
18. Gunn, J. E. *et al.* The Sloan Digital Sky Survey photometric camera. *Astron. J.* **116,** 3040–3081 (1998).
19. Pier, J. R. *et al.* Astrometric calibration of the Sloan Digital Sky Survey. *Astron. J.* **125,** 1559–1579 (2003).
20. Hogg, D. W., Finkbeiner, D. P., Schlegel, D. J. & Gunn, J. E. A photometricity and extinction monitor at the Apache Point Observatory. *Astron. J.* **122,** 2129–2138 (2001).
21. Smith, J. A. *et al.* The $u'g'r'i'z'$ standard-star system. *Astron. J.* **123,** 2121–2144 (2002).
22. Fukugita, M. *et al.* The Sloan Digital Sky Survey photometric system. *Astron. J.* **111,** 1748–1756 (1996).
23. Blanton, M. R. *et al.* An efficient targeting strategy for multiobject spectrograph surveys: The Sloan Digital Sky Survey "tiling" algorithm. *Astron. J.* **125,** 2276–2286 (2003).
24. Richards, G. T. *et al.* Spectroscopic target selection in the Sloan Digital Sky Survey: The quasar sample. *Astron. J.* **123,** 2945–2975 (2002).
25. Oguri, M., Taruya, A., Suto, Y. & Turner, E. L. Strong gravitational lensing time delay statistics and the density profile of dark halos. *Astrophys. J.* **568,** 488–499 (2002).
26. Kashikawa, N. *et al.* FOCAS: The Faint Object Camera and Spectrograph for the Subaru Telescope. *Publ. Astron. Soc. Jpn* **54,** 819–832 (2002).
27. Cao, L., Wei, J.-Y. & Hu, J.-Y. High X-ray-to-optical flux ratio RASS-BSC sources. I. The optical identification. *Astron. Astrophys. Suppl.* **135,** 243–253 (1999).
28. Keeton, C. R. Computational methods for gravitational lensing. Preprint at ⟨http://xxx.lanl.gov/astro-ph/0102340⟩ (2001).
29. Oke, J. B. *et al.* The Keck Low-Resolution Imaging Spectrometer. *Publ. Astron. Soc. Pacif.* **107,** 375–385 (1995).
30. Miyazaki, S. *et al.* Subaru prime focus camera—Suprime-Cam. *Publ. Astron. Soc. Jpn* **54,** 833–853 (2002).

Acknowledgements Funding for the creation and distribution of the SDSS Archive has been provided by the Alfred P. Sloan Foundation, the Participating Institutions, the National Aeronautics and Space Administration, the National Science Foundation, the US Department of Energy, the Japanese Monbukagakusho, and the Max Planck Society. The SDSS website is http://www.sdss.org/. The SDSS is managed by the Astrophysical Research Consortium (ARC) for the Participating Institutions. The Participating Institutions are The University of Chicago, Fermilab, the Institute for Advanced Study, The Japan Participation Group, The Johns Hopkins University, Los Alamos National Laboratory, the Max-Planck-Institute for Astronomy (MPIA), the Max-Planck-Institute for Astrophysics (MPA), New Mexico State University, University of Pittsburgh, Princeton University, the United States Naval Observatory, and the University of Washington. This Letter is based in part on data collected at the Subaru telescope, which is operated by the National Astronomical Observatory of Japan, W. M. Keck Observatory, which is operated as a scientific partnership among the California Institute of Technology, the University of California, and the National Aeronautics and Space Administration, and the Apache Point Observatory (APO) 3.5-m telescope, which is owned and operated by the Astrophysical Research Consortium. Part of this work was performed under the auspices of the U.S. Department of Energy at the University of California Lawrence Livermore National Laboratory.

Competing interests statement The authors declare that they have no competing financial interests.

Correspondence and requests for materials should be addressed to N.I. (inada@utap.phys.s.u-tokyo.ac.jp).

Subatomic movements of a domain wall in the Peierls potential

K. S. Novoselov[1], A. K. Geim[1], S. V. Dubonos[3], E. W. Hill[2] & I. V. Grigorieva[1]

[1]*Department of Physics,* [2]*Department of Computer Sciences, University of Manchester, Manchester M13 9PL, UK*
[3]*Institute for Microelectronics Technology, 142432 Chernogolovka, Russia*

The discrete nature of crystal lattices plays a role in virtually every material property. But it is only when the size of entities hosted by a crystal becomes comparable to the lattice period—as occurs for dislocations[1–3], vortices in superconductors[4–6] and domain walls[7–9]—that this discreteness is manifest explicitly. The associated phenomena are usually described in terms of a background Peierls 'atomic washboard' energy potential, which was first introduced for the case of dislocation motion[1,2] in the 1940s. This concept has subsequently been invoked in many situations to describe certain features in the bulk behaviour of materials, but has to date eluded direct detection and experimental scrutiny at a microscopic level. Here we report observations of

© 2003 Nature Publishing Group

the motion of a single magnetic domain wall at the scale of the individual peaks and troughs of the atomic energy landscape. Our experiments reveal that domain walls can become trapped between crystalline planes, and that they propagate by distinct jumps that match the lattice periodicity. The jumps between valleys are found to involve unusual dynamics that shed light on the microscopic processes underlying domain-wall propagation. Such observations offer a means for probing experimentally the physics of topological defects in discrete lattices—a field rich in phenomena that have been subject to extensive theoretical study[10–12].

In magnetic materials, a domain wall (DW) has to pass through different spin configurations as it moves from one atomic plane to another[7–14]. Figure 1a shows two principal spin configurations of a DW in a simple lattice—these configurations exhibit the maximum and minimum energy, and correspond to the centre of the wall lying respectively at and between atomic planes. This spatial variation of the wall's energy is generally referred to as the Peierls potential. Its amplitude depends critically on the ratio between the DW's width δ and the lattice periodicity d and, realistically, the Peierls potential is only observable for $\delta/d < 10$. For larger δ/d, the potential becomes so small ($\ll$1 G) that pinning on defects should conceal it completely. The vast theoretical and experimental evidence gathered over several decades and based on studies of bulk properties of magnetic alloys has confirmed the existence of the magnetic Peierls potential, with probably the most definite conclusions drawn from measurements of magnetic viscosity (for example, see refs 14–16). However, no experiment has yet been capable of directly detecting propagation through the magnetic (or any other) Peierls potential. In the present work, we revisit the Peierls potential by using a state-of-the-art technique of ballistic Hall micromagnetometry, previously used in studies of superconducting vortices[17,18] and now adapted to the detection of DW movements. The approach allows us to resolve subatomic changes in the position of individual micrometre-sized segments of DWs and study their inter- and intra-Peierls valley movements.

For our studies, we have chosen thin films of yttrium-iron garnet, $(YBi)_3(FeGa)_5O_{12}$ (YIG), which combine relatively narrow walls ($\delta \approx 11$ nm at liquid-helium temperatures) with a large unit cell of size $a \approx 1.24$ nm, and provide $\delta/d \approx 6$ (Methods). Equally important is the high crystal quality of our samples[19–21], manifested in a coercivity of $<$0.1 G at room temperature and $<$10 G at liquid-helium temperatures, such that obscuring effects due to pinning on defects are relatively small. The YIG films have perpendicular magnetization and a domain structure shown in Fig. 1b for the case of room temperature. At low temperatures, the domain structure becomes pronouncedly triangular with long straight DWs. A submillimetre piece of the film was placed in immediate contact with the surface of a device consisting of micrometre-sized Hall sensors made from a two-dimensional electron gas (2DEG) following the microfabrication procedure described in refs 17 and 18 (Fig. 1b). Hall sensors in our experiments play the role of highly sensitive position detectors, which provide a spatial resolution of $<$1 Å with respect to DW movements. Their operation (explained in Methods) relies on the high sensitivity of such probes to changes in magnetic flux Φ induced by DW movements inside the central area of a Hall cross[17,18,22–26]. For brevity, we discuss only experiments where the studied DWs were aligned parallel with the Hall device and moved in {110} directions. In this well defined geometry, changes in the wall position Δx can be calculated directly from

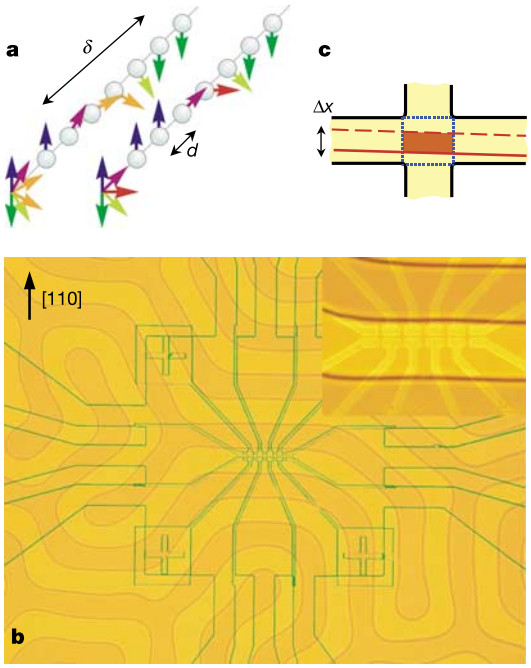

Figure 1 Experimental structures and devices. **a**, Principal spin configurations for a narrow Bloch wall: its centre either coincides with one of the atomic planes (right) or lies between them (left). The fan diagrams show the orientation of individual spins, looking in the direction perpendicular to the DW. **b**, The micrographs show a set of micrometre-sized Hall probes placed on top of a ferromagnetic garnet. Edges of the 2DEG mesa are seen as green lines on the micrograph. The image overlays a photograph of the domain structure taken in transmitted polarized light at room temperature. The inset magnifies the central part of the experimental structure. The scale is given by the domains' width of ~14 μm and the size of Hall probes (1.5 μm). By measuring simultaneously the response at different Hall crosses, we ensured that at low temperatures the studied DWs were parallel to the set of sensors as the photograph shows and moved as rigid planes (Methods). **c**, The drawing illustrates that a shift in the average position of a wall Δx induces a change in flux $\Delta\Phi$ inside the sensitive area marked by the dotted lines[17,22]. This leads to a linear change in Hall resistance, which was recorded in the experiments.

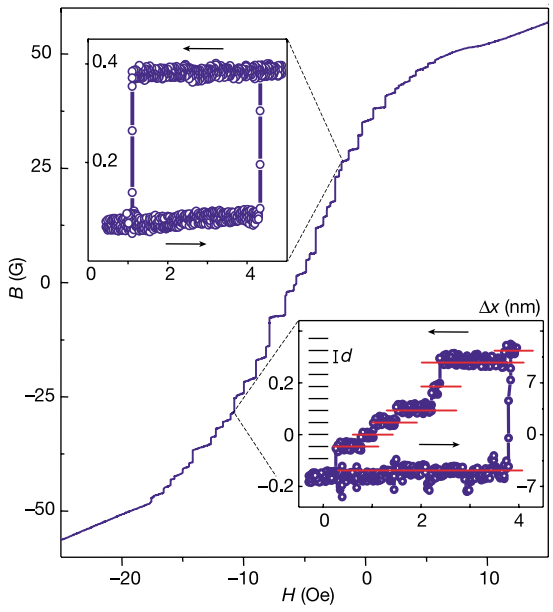

Figure 2 Nanometre movements of domain walls over submicrometre distances. Main panel, a typical Hall response measured by a 1.5-μm Hall cross as a domain wall slowly creeps from one of its sides to the other ($T = 0.5$ K). For convenience, the Hall response is given in terms of the average local field B inside the cross, which is calculated by using the measured Hall coefficient. The insets show examples of local hysteresis loops; abscissa, ΔH (Oe); left-hand ordinate, ΔB (G), right-hand ordinate (lower inset only), Δx (nm). The red lines are guides to the eyes, indicating constant positions of the DW.

© 2003 Nature Publishing Group

the measured Hall signal, without using any unknown parameters (Methods).

To move a DW, we slowly varied the external field H applied perpendicular to the garnet film. Figure 2 shows a typical example of changes in local field B detected by a Hall sensor as a DW crosses it from one side to the other. We see that B changes its sign, which reflects the change in polarity of the domain above the sensor, and $B = 0$ corresponds to the state where the wall lies exactly in the middle. The overall shape of the transition curve is in good agreement with a simple theory[21]. Overlaid on this universal behaviour, we see a number of small sample- and sweep-dependent steps, indicating that a DW does not move smoothly but covers micrometre-long distances in a series of small jumps. Such jumps have previously been studied by several techniques (for example, refs 27–29), and are usually referred to as Barkhausen noise. A typical step in Fig. 2 corresponds to a wall moving by 10–50 nm. While a DW was located within the Hall cross, we could reverse a field sweep to investigate the local coercivity of the wall (left inset in Fig. 2). Such hysteresis loops are usually reproducible for many field cycles, and we attribute them to pinning on individual defects[21,28].

In addition to the above behaviour, the high resolution of the 2DEG micromagnetometry allowed us to discern very small DW jumps (right inset in Fig. 2), which stood out from the 'ordinary' jumps for two reasons. First, they matched closely the lattice periodicity in the direction of DW travel $\langle 110 \rangle$ ($d = 2^{1/2}a \approx 1.75$ nm) and, second, they were practically the only jumps observed in the range below ~10 nm. The use of statistical analysis techniques (which is standard practice in, for example, particle physics) shows that—with a confidence level of 94%—the data shown in the right inset of Fig. 2 correspond to an event comprising several steps of equal length (four single and three double steps), where the length of a single step is d. To obtain further proof that such steps indeed reveal jumps between equivalent crystal lattice positions, we carried out the complementary experiments described below.

As a DW moves through a crystal, it interacts with a large number of pinning sites and becomes bent and strained in the process. We can generally expect that a strained wall would jump between strong pinning sites without being affected by the weaker ones. This is clearly seen by magnetic force microscopy (at room temperature). To release the strain, we demagnetized the sample by applying an a.c. magnetic field with an amplitude h gradually decreasing from ~5 G to zero, while a constant field H kept the wall close to the centre of the probe. This proved to be a critical improvement: in the demagnetized state, DWs started to propagate via clear quantized jumps matching the lattice periodicity. The distance between the equivalent sites was measured to be 1.6 ± 0.2 nm, in agreement with the Peierls potential periodicity $d = 1.75$ nm. Figure 3 shows an example of such behaviour, which leaves no doubt of the presence of a periodic atomic landscape impeding DW movements.

From Fig. 3, we can also estimate that it requires a field of ~1 G to move a DW out of a well created by adjacent crystal planes (that is, intrinsic pinning is several times weaker than pinning on a typical defect in our garnets; see Fig. 2). Further experiments yielded a value of the intrinsic coercive field $H_C \approx 0.7$ G at $T < 10$ K. The theory of the magnetic Peierls potential predicts H_C to be of the order of[13–15]

$$H_C \approx C(A/d^2 M_S)\exp(-\pi\delta/d)$$

where $C \approx 10^3$ (ref. 13) and M_S is the saturation magnetization. Taking into account the exponential dependence of H_C on A and K (Methods), which are known to ~10% accuracy, the formula yields H_C in the range from 0.1 to 5 G, in agreement with the experiment.

In addition to the detection of the Peierls potential, we have studied its shape, which is predicted to be sinusoidal[7,13]. This prediction implies that a DW should remain somewhat mobile within Peierls valleys—that is, not pinned completely. Such intra-valley movements are expected to be ~1 Å and, therefore, could not be resolved in our d.c. magnetization data (compare Fig. 3). To gain information about the finest DW movements, we measured local a.c. susceptibility χ (a.c. measurements provide a higher flux sensitivity, and hence a higher spatial resolution). To this end, in addition to the d.c. field H that controls DW's position, we applied an oscillating field h and measured an a.c. signal generated by oscillatory movements of a DW. Changes in χ show how the mobility of a DW varies with its position inside a Peierls valley. Using this approach, we confirmed that a domain wall could indeed move near the bottom of a valley, and the detected a.c. signal corresponded to an average shift of a DW by up to ~0.5 Å. In addition to this, however, a.c. measurements revealed strikingly

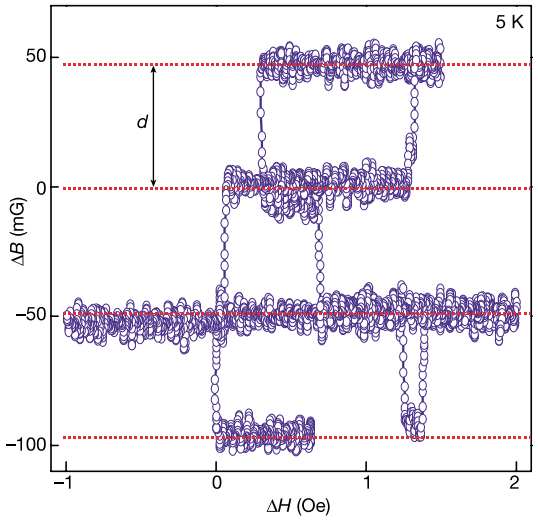

Figure 3 Jumps of a domain wall between equivalent lattice sites. The data were taken during a very slow sweep (~1 h), which was required to achieve the subatomic resolution. For such time intervals, relaxation processes lead to irreproducible changes in the domain structure, usually far away from the detection site (this can be seen as occasional DW jumps at a constant H). On the graph, this results in the same position of a DW for different values of H. For clarity, we subtracted a small smooth background in B associated with changes in the local stray field induced by other domains.

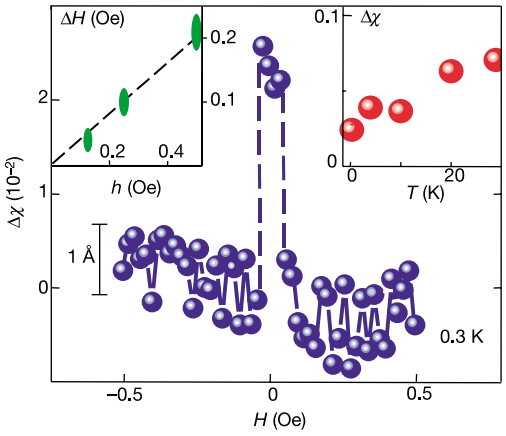

Figure 4 Domain wall on the Peierls ridge. Main panel, changes in local a.c. susceptibility χ while d.c. field H moves the wall from one Peierls valley to the next (a.c. field has amplitude 0.5 G and frequency 8 Hz). We subtracted a constant background due to the Hall response induced directly by the a.c. field. The slight variation of χ seen on the curve away from the transient state is not reproducible for different walls and after thermal cycling. The insets show the dependence of the width ΔH of the transient state on h, and the dependence of its amplitude $\Delta\chi$ on temperature.

© 2003 Nature Publishing Group

unusual DW dynamics, in qualitative disagreement with the behaviour expected for an object moving in a tilted sinusoidal potential.

One of the most notable features that we observed is a large, well-reproduced peak in DW mobility (Fig. 4). Here, zero H corresponds to a DW position in the middle between two adjacent Peierls valleys, as simultaneously detected in the d.c. magnetization signal (the latter shows a smeared transition between two DW positions separated by d). The peak has abrupt edges (shown by dashed lines in Fig. 4); that is, above a certain value of H the oscillating wall suddenly falls into a neighbouring Peierls valley and becomes locked there. When h was switched off for a few seconds at a constant H close to one of the peak's edges, the transient mobile state did not recover on switching the modulation back. This indicates that it requires a time of ~1 s for the wall to become locked in a Peierls valley. With decreasing h from 0.5 to 0.1 G, both the width and the amplitude of the peak shrink linearly (inset in Fig. 4). The observed behaviour suggests that an a.c. field stabilizes a DW in what should be an intrinsically unstable state between two Peierls valleys.

We can interpret the transient state as the centre of a DW sitting effectively on a Peierls ridge, kept there by an oscillating magnetic force. This situation closely resembles the so-called reversed pendulum, which can be stabilized in the unstable upside-down position by an oscillating force[30,31]. This analogy allows us to describe the observed resonance semiquantitatively but does not provide a microscopic picture. To this end, we invoke the well-known 'kink' model[2,14], where a DW moves between Peierls valleys via a process where at first only a submicrometre segment of a DW (a jog) moves to the next valley. Spreading the boundary of such a jog along the wall eventually leads to the relocation of the whole DW. It is plausible that a.c. modulation could stabilize the jog so that its boundaries move back and forth inside the sensitive area of a Hall cross without collapsing, until changes in H extend the jog outside this area, where it eventually becomes pinned. Indeed, the maximum value of $\Delta\chi$ (observed at 30 K and 0.5 G) corresponds to movements of a DW by $\Delta x \approx 1$ nm; that is, as if nearly the whole segment of the wall inside the Hall cross swings between adjacent valleys.

The single-jog model provides a sensible description for the behaviour shown in Fig. 4, as well as for the majority of other a.c. susceptibility results (to be reported elsewhere). However, the origin of the long characteristic times remains puzzling. Moreover, we believe that the kink/jog picture may no longer be justifiable for the case of $\Delta x \ll \delta$ as, on this scale, the spin configuration of a DW changes (the DW can 'breathe') and we cannot simply refer to an average shift of a DW as a whole. We believe that the detected transient state indicates some internal modes being excited inside a DW when it is 'softened' and ready to move from one valley to another.

Further experimental and theoretical work is required to understand atomic-scale DW dynamics. This physics has been extensively discussed in theory (for example, solitons on discrete lattices[10–12]), but has not until now been accessible in a direct experiment to allow the testing of a variety of theoretical models. The present results demonstrate the possibility of studying the physics of domain walls at a new level of experimental resolution, and in a controlled and reproducible manner. This development is likely to lead not only to refinements of the existing models, but also to a greater depth of understanding of fundamental and technologically important phenomena governed by movements of domain walls. □

Methods

Samples

We studied a 10-μm-thick $(YBi)_3(FeGa)_5O_{12}$ film grown in the [111] direction. The material has a saturation magnetization $4\pi M_s \approx 200$ G, an exchange energy $A \approx 1.8 \times 10^{-7}$ erg cm^{-1} and, below 10 K, its crystal anisotropy $K \approx 1.4 \times 10^6$ erg cm^{-3} yields a wall thickness $\delta = \pi(A/K)^{1/2} \approx 11$ nm. The above values were found with accuracy ~10%.

Owing to in-plane crystal anisotropy, DWs tend to lie in three equivalent planes, {110}. This crystallographic alignment is already seen at 300 K (Fig. 1b), and becomes stronger at lower temperatures as the anisotropy increases. There, domain walls become straight over distances of ~1 mm. Using alignment marks, we placed our 2DEG sensors inside a chosen area of a YIG film with many parallel domains and aligned the sensors parallel to them, that is, perpendicular to one of ⟨110⟩ axes. The spacing between the garnet and 2DEG was measured to be less than 100 nm (ref. 21). We restricted the reported experiments to temperatures below 30 K, mainly because of thermally activated relaxation processes, which led to irreproducible changes in the domain structure and did not allow accurate measurements that require slow sweeps of magnetic field.

There are two periodic sets of equivalent crystallographic positions for a {110} DW, which are separated by b and $2b$ (where $b = a/\sqrt{2}$ is the distance between the nearest basal planes). They require the translation of wall's spin configuration in directions ⟨001⟩ and ⟨110⟩, respectively, and involve different exchange interactions[13]. Both periods should contribute to the Peierls potential, but because of the exponential dependence on δ/d only the longest periodicity $d = 2a/\sqrt{2} \approx 1.75$ nm can be expected to remain observable. Our measurements did find this periodicity, but it remains unclear why a DW could not avoid the observed Peierls barriers by exploiting 'the third dimension' (that is, moving by two smaller oblique jumps in ⟨001⟩ rather than by the straight jumps perpendicular to the DW's plane). We finally note that our analysis ignores the complex unit cell structure of garnets, which may also play some role.

Micromagnetometers

Submicrometre Hall probes made from a 2DEG were used as position detectors of a domain wall. When a DW enters the sensitive area of a probe, its response R_H starts changing. A shift Δx in the DW's position leads to a change in magnetic field B and flux Φ through the Hall cross (Fig. 1c), which in turn induces a Hall response such that $\Delta R_H = \alpha\Delta\Phi = \beta\Delta x$ (refs 17, 22). The second part of the equation assumes that a DW is straight within the sensitive area of the Hall cross. This is justified for the reported experiments because we could simultaneously measure R_H at different crosses and, at low T, found a nearly perfect correlation between movements of DWs detected by neighbouring Hall crosses[21]. This indicates that DWs move as fairly rigid objects, so that their large segments (up to 10 μm in size for $T < 10$ K) shift as a whole (that is, without bending). α and β are found experimentally[17,21,22] and, therefore, changes in R_H can be translated in DW movements without any fitting parameters.

We used Hall sensors made from a high-mobility 2DEG because of their exceptional sensitivity to flux variations $\Delta\Phi$ on a submicrometre scale[17]. At temperatures $T < 80$ K, such sensors effectively work as fluxmeters and are capable of resolving $\Delta\Phi \approx 10^{-4}\,\phi_0$, where ϕ_0 is a flux quantum. This technique has previously been used and fully described in studies of submicrometre superconducting[17,18] and ferromagnetic[23–26] particles. In the context of the present work, we have exploited this unique flux sensitivity of 2DEG sensors to achieve a subatomic resolution in the average position of individual DWs. Indeed, if a DW passes the whole width w of a cross, Φ changes by several ϕ_0 (for the given value of M_s in our garnets). On the other hand, as we can resolve $\Delta\Phi \approx 10^{-4}\phi_0$, this corresponds to a shift of a DW by $\Delta x \approx w(\Delta\Phi/\phi_0) \approx 1$ Å. Note that many magnetic materials have larger values of M_s and, hence, the magnetometers should provide even higher spatial resolution (<0.1 Å). We mainly used 2DEG crosses with $w \approx 1$–2 μm because, in our experience, they exhibit low noise and allow the maximum spatial resolution.

Received 7 July; accepted 29 October 2003; doi:10.1038/nature02180.

1. Peierls, R. E. The size of a dislocation. *Proc. Phys. Soc.* **52,** 34–37 (1940).
2. Nabarro, F. R. N. Dislocations in a simple cubic lattice. *Proc. Phys. Soc.* **59,** 256–272 (1947).
3. Kolar, H. R., Spence, J. C. H. & Alexander, H. Observation of moving dislocation kinks and unpinning. *Phys. Rev. Lett.* **77,** 4031–4034 (1996).
4. Ivlev, B. I. & Kopnin, N. B. Flux creep and flux pinning in layered high-temperature superconductors. *Phys. Rev. Lett.* **64,** 1828–1830 (1990).
5. Oussena, M., deGroot, P. A. J., Gagnon, R. & Taillefer, L. Lock-in oscillations in magnetic hysteresis curves of $YBa_2Cu_3O_{7-x}$ single crystals. *Phys. Rev. Lett.* **72,** 3606–3609 (1994).
6. Kleiner, R., Steinmeyer, F., Kunkel, G. & Müller, P. Intrinsic Josephson effects in $Bi_2Sr_2CaCu_2O_8$ single crystals. *Phys. Rev. Lett.* **68,** 2394–2397 (1992).
7. Barbara, B. Propriétés des parois étroites dans les substances ferromagnétiques à forte anisotropie. *J. Phys* **34,** 1039–1046 (1973).
8. van den Broek, J. J. & Zijlstra, H. Calculation of intrinsic coercivity of magnetic domain walls in perfect crystals. *IEEE Trans. Magn.* **7,** 226–230 (1971).
9. Egami, T. & Graham, C. D. Jr Domain walls in ferromagnetic Dy and Tb. *J. Appl. Phys.* **42,** 1299–1300 (1971).
10. Aubry, S. Devils staircase and order without periodicity in classical condensed matter. *J. Phys.* **44,** 147–162 (1983).
11. Braun, O. M. & Kivshar, Y. S. Nonlinear dynamics of the Frenkel-Kontorova model. *Phys. Rep.* **306,** 2–108 (1998).
12. Bishop, A. R. & Lewis, W. F. A theory of intrinsic coercivity in narrow domain wall materials. *J. Phys. C* **12,** 3811–3825 (1979).
13. Hilzinger, H. R. & Kronmüller, H. Spin configuration and intrinsic coercive field of narrow domain walls in Co_5R-compounds. *Phys. Status Solidi* **54,** 593–604 (1972).
14. Egami, T. Theory of intrinsic magnetic after-effect. *Phys. Status Solidi* **19,** 747–758 (1973).
15. Arnaudas, J. I., del Moral, A. & Abell, J. S. Intrinsic coercive field in pseudobinary cubic intermetallic compounds. *J. Magn. Magn. Mater.* **61,** 370–380 (1986).
16. Musbniskov, N. V., Andreev, A. V., Korolyov, A. V. & Shiokawa, Y. Magnetic viscosity in a UPtAl single crystal. *J. Alloys Comp.* **305,** 188–193 (2002).
17. Geim, A. K. *et al.* Ballistic Hall micromagnetometry. *Appl. Phys. Lett.* **71,** 2379–2381 (1997).
18. Geim, A. K. *et al.* Phase transitions in individual sub-micrometre superconductors. *Nature* **390,** 259–262 (1997).
19. Pisarev, R. V. *et al.* Optical second-harmonic generation in magnetic garnet thin films. *J. Phys.* **5,** 8621–8628 (1993).

© 2003 Nature Publishing Group

20. Pavlov, V. V., Pisarev, R. V., Kirilyuk, A. & Rasing, T. Observation of a transversal nonlinear magneto-optical effect in thin magnetic garnet films. *Phys. Rev. Lett.* **78,** 2004–2007 (1997).
21. Novoselov, K. S., Geim, A. K., van der Berg, D., Dubonos, S. V. & Maan, J. C. Domain wall propagation on nanometer scale: coercivity of a single pinning center. *IEEE Trans. Magn.* **38,** 2583–2585 (2002).
22. Peeters, F. M. & Li, X. Q. Hall magnetometer in the ballistic regime. *Appl. Phys. Lett.* **72,** 572–574 (1998).
23. Kent, A. D., von Molnar, S., Gider, S. & Awschalom, D. D. Properties and measurement of scanning tunneling microscope fabricated ferromagnetic particle arrays. *J. Appl. Phys.* **76,** 6656–6660 (1994).
24. Li, Y. Q. *et al.* Hall magnetometry on a single iron nanoparticle. *Appl. Phys. Lett.* **80,** 4644–4646 (2002).
25. Hengstmann, T. M., Grundler, D., Heyn, C. & Heitmann, D. Stray-field investigation on permalloy nanodisks. *J. Appl. Phys.* **90,** 6542–6544 (2001).
26. Schuh, D., Biberger, J., Bauer, A., Breuer, W. & Weiss, D. Hall-magnetometry on ferromagnetic dots and dot arrays. *IEEE Trans. Magn.* **37,** 2091–2093 (2001).
27. Vergne, R., Cotillard, J. C. & Porteseil, J. L. Some statistical aspects of magnetization processes in ferromagnetic bodies—motion of a single 180-degrees Bloch wall in an imperfect crystalline medium. *Rev. Phys. Appl.* **16,** 449–476 (1981).
28. Wunderlich, J. *et al.* Influence of geometry on domain wall propagation in a mesoscopic wire. *IEEE Trans. Magn.* **37,** 2104–2107 (2001).
29. Kim, D. H., Choe, S. B. & Shin, S. C. Direct observation of Barkhausen avalanche in Co thin films. *Phys. Rev. Lett.* **90,** 087203 (2003).
30. Magnus, K. *Vibrations* (Blackie & Son, London, 1965).
31. Acheson, D. *From Calculus to Chaos* (Oxford Univ. Press, Oxford, 1997).

Acknowledgements This research was supported by the EPSRC (UK). We thank S. Gillott and M. Sellers for technical assistance and J. Steeds for advice on dislocation motion. S.V.D. also acknowledges support from Russian Ministry of Science and Technology.

Competing interests statement The authors declare that they have no competing financial interests.

Correspondence and requests for materials should be addressed to A.K.G. (geim@man.ac.uk).

Subwavelength-diameter silica wires for low-loss optical wave guiding

Limin Tong[1,2], Rafael R. Gattass[1], Jonathan B. Ashcom[1]*, Sailing He[2], Jingyi Lou[2], Mengyan Shen[1,3], Iva Maxwell[1] & Eric Mazur[1]

[1]*Department of Physics and Division of Engineering and Applied Sciences, Harvard University, Cambridge, Massachusetts 02138, USA*
[2]*Centre for Optical and Electromagnetic Research and Department of Physics, Zhejiang University, Hangzhou 310027, China*
[3]*Department of Physics, Graduate School of Science, Tohoku University, Sendai, Miyagi 9808578, Japan*

* Present address: Lincoln Laboratory, Massachusetts Institute of Technology, Lexington, Massachusetts 02420, USA

Silica waveguides with diameters larger than the wavelength of transmitted light are widely used in optical communications, sensors and other applications[1–3]. Minimizing the width of the waveguides is desirable for photonic device applications, but the fabrication of low-loss optical waveguides with subwavelength diameters remains challenging because of strict requirements on surface roughness and diameter uniformity[4–7]. Here we report the fabrication of subwavelength-diameter silica 'wires' for use as low-loss optical waveguides within the visible to near-infrared spectral range. We use a two-step drawing process to fabricate long free-standing silica wires with diameters down to 50 nm that show surface smoothness at the atomic level together with uniformity of diameter. Light can be launched into these wires by optical evanescent coupling. The wires allow single-mode operation, and have an optical loss of less than 0.1 dB mm^{-1}. We believe that these wires provide promising building blocks for future microphotonic devices with subwavelength-width structures.

The fabrication of thin silica wires was first investigated in the nineteenth century, when the mechanical properties of the wires were studied, but their optical properties and applications remained uninvestigated[8,9]. It was not until a century later that researchers began to investigate the optical applications of silica wires made by drawing high-purity glass fibres from a laser-heated melt[10–14]. With a diameter of more than one micrometre, these silica wires allow multimode waveguiding of visible and infrared light. Submicrometre wires allow single-mode operation, but both theoretical and experimental results show that the laser power required for drawing silica submicrometre- or nanometre-diameter wires (SMNWs) with a uniform diameter is impractically large[14,15]. When drawing wires from a flame-heated melt, turbulence and convection make it difficult to control the temperature gradient in the drawing region, and consequently size uniformity is difficult to maintain when the wire diameter is reduced to less than one micrometre. Silica nanowires with diameters ranging from ten to several hundred nanometres have recently been obtained with other methods[16–18], but the diameter fluctuation and sidewall roughness of those wires makes them unsuitable for low-loss optical wave guiding.

Here we introduce a two-step drawing process for fabricating long uniform silica SMNWs by a flame-heated fibre drawing method. First, we use a flame to draw a silica fibre to a micrometre-diameter wire. Second, to obtain a steady temperature distribution in the drawing region while further reducing the wire diameter, we use a tapered sapphire fibre with a tip diameter of about 80 μm to absorb the thermal energy from the flame (Fig. 1). The sapphire fibre taper, which is fabricated using laser-heating growth method[19], confines the heating to a small volume and helps maintain a steady temperature distribution during the drawing. One end of a micrometre-diameter silica wire is placed horizontally on the sapphire tip, and the flame is adjusted until the temperature of the tip is just above the drawing temperature (about 2,000 K). We then rotate the sapphire tip around its axis of symmetry to wind the silica wire around the tip. The wire coil is moved about 0.5 mm out of the flame to prevent melting and the wire is then drawn perpendicular to the axis of the sapphire tip in the horizontal plane at a speed of 1–10 mm s^{-1} to form a SMNW.

Using this technique, we obtained silica SMNWs with diameters down to 50 nm and lengths up to tens of millimetres. Figure 2a shows a scanning electron microscope (SEM) image of a 4-mm-long wire with a diameter of 260 nm; the wire is roughly coiled up to show its length. The maximum diameter variation ΔD is about 8 nm over the 4-mm length L of the wire, giving $\Delta D/L = 2 \times 10^{-6}$. The excellent uniformity of wires with diameters ranging from 50 to 1,100 nm can also be seen in Fig. 2b–d. Higher-magnification transmission electron microscope (TEM) images of a 240-nm-

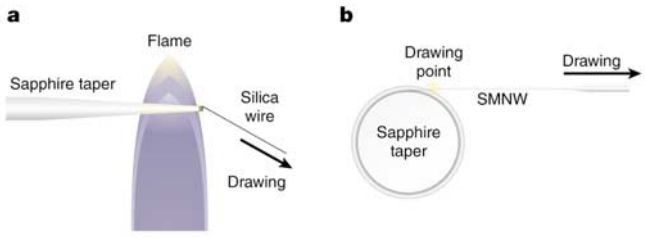

Figure 1 The second step in the fabrication process of silica submicrometre- and nanometre wires (SMNWs). **a**, Schematic diagram of the drawing of the wire from a coil of micrometre-diameter silica wire wound around the tip of a sapphire taper. The sapphire taper is heated with a CH_3OH torch with a nozzle diameter of about 6 mm. The wire is drawn in a direction perpendicular to the sapphire taper. **b**, Magnified view of the drawing process. The sapphire taper ensures that the temperature distribution in the drawing region remains steady.

© 2003 Nature Publishing Group